Electronic Supplementary Material (ESI) for Sustainable Energy & Fuels.
This journal is © The Royal Society of Chemistry 2020

Essential Supplementary Information (ESI)

Enhanced electrocatalytic and supercapacitive performance using synergistic effect of defect-rich N/S co-doped hierarchical porous carbon

Mohammad Shaad Ansari, Thomas Nesakumar Jebakumar Immanuel Edison, and Yong Rok Lee*

School of Chemical Engineering, Yeungnam University, Gyeongsan, Gyeongbuk-do 38541, Republic of Korea.

*Corresponding author: Tel: +82-53-810-2529. Fax: 82-53-810-4631. E-mail: yrlee@yu.ac.kr (Yong Rok Lee).

Table of Contents

I. Chemical structure of bio-mass derived precursor

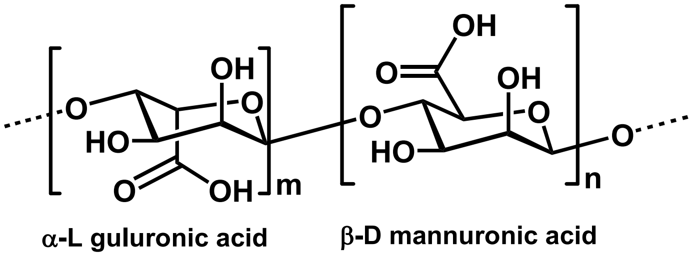

Figure S1. Chemical structure of biomass derived carbon precursor “alginic acid”.

II. Materials and reagents

All chemicals used in the synthetic route and characterizations were used without any further purification. Alginic Acid, sulfanilic acid, potassium hydroxide (KOH), polyvinylidene fluoride (PVDF), N-methyl-2-pyrrolidone (NMP) were purchased from Sigma-Aldrich, Korea. Hydrochloric acid (HCl), sulfuric acid (H_2SO_4) was purchased from Daejung Chemicals Korea. Stainless steel (SS) was used as current collecting electrode, are obtained from MTI Korea. High grade double distilled water is used as an electrolyte medium.

III. Materials characterization

Crystal phase purity of as-synthesized electrocatalysts was analysed by powder X-ray diffraction (PXRD) measurements using PANalytical X’Pert^3 MRD diffractometer with Cu Ka radiation (l = 1.54 Å) having liquid nitrogen cooled germanium solid-state detector and operating at a voltage of 40 kV and current of 30 mA. Scan rate was fixed at 0.05 °/s for recording the PXRD patterns in a wide range of 2θ (i.e., 10-80°). Morphological features of the samples were determined by scanning electron microscopy (SEM) analysis using Hitachi S-4800 FE-SEM coupled with EDS, operated at the voltages of 10 kV. Microstructural properties of materials were investigated by transmission electron microscopy (TEM) measurements using FEI Tecnai TF20 HR-TEM instruments. For determination of chemical composition, X-ray photoelectron spectroscopy (XPS) was performed using a Thermo-Scientific K-Alpha spectrometer. Baseline of all spectra was corrected using the instrument software. Scanning transmission electron microscopy (STEM) analysis was conducted to find the elemental mapping of the samples using FEI Tecnai TF20 HR-TEM instruments. Nitrogen (N_2) adsorption-desorption isotherms were performed at liquid N_2 temperature to estimate the Brunauer-Emmett-Teller (BET) surface area and porosity profile of as-synthesized samples using Micromeritics ASAP2000. Prior to the surface area analysis, samples were degassed at 150 °C for 4 h. Chemical structure of both samples were evaluated by FT-IR analyses using Perkin-Elmer spectrum two FT-IR spectrophotometer with attenuated total reflectance (ATR) kit. Raman spectra of all materials were recorded on a thermoscientific DXR SmartRaman spectrometer with laser excitation at 532 nm while Thermogravimetric analysis (TGA) was carried out on a NETZSCH STA409PC instrument under N_2 atmosphere at a heating rate of 10 °C min^{-1} at the core research support center for natural products and medical materials, Yeungnam University. All electro-chemical measurements were performed using Corrtest-CS350 electrochemical analyzer with Cview and Zview software.

IV. Fabrication of working electrode and electrochemical measurements

For fabrication of the working electrode, stainless steel having active surface area (1*1 cm^2) was pre-treated with 1M KOH for 30 min, followed by washing with deionized water and dried in hot air oven. Homogenous paste of active electrode materials was prepared by mixing the as-synthesized material with the binder polyvinylidene fluoride (PVDF) in the weight ratio of 8:2 in 2 mL of 1-methyl-2-pyrrolidone (NMP). After that, this paste was drop casted over stainless steel having predefined active area and dried in a hot air oven at 100 °C for overnight. For supercapacitor studies, active mass of deposited active material was estimated by subtracting the weight of loaded electrode from the blank electrode, which is found to be 4.24 mg/cm^2.

Electrochemical measurements of the fabricated electrode were conducted on an electrochemical analyzer (Corrtest-CS350) in a three-electrode system, using aqueous 1M H_2SO_4 as electrolyte, Pt as a counter electrode and Ag/Ag_2SO_4 as a reference electrode. Linear sweep voltammetry (LSV) was carried out from 0.20 V to -1.3 V vs. Ag/Ag_2SO_4 at the scan rate of 10 mV/s and subsequently Tafel analyses were also performed using same parameters. Cyclic voltammetry (CV) and Galvanostatic charge-discharge (GCD) analyses were carried out within the potential range of -0.25 to 0.40 V vs Ag/Ag_2SO_4 at different scan rate 200, 150, 100, 90, 80, 70, 60, 60, 50, 40, 30, 20, 10 and 5mV/s and different current densities values of 0.5, 1, 2, 3, 4, 5 and 10 A/g, respectively. Electrochemical impedance spectroscopy (EIS) measurements for both samples were carried out at potential (-1 V vs. Ag/Ag_2SO_4) in a frequency range of 0.01 to 10^4 Hz with an amplitude of 5 mV. Stability of heteroatom-doped hierarchical porous carbon based electrode was tested by employing chronopotentiometry at a constant current of 10 mA/cm^2 for 10 h. As-applied potential using Ag/Ag_2SO_4 reference electrode were converted to the reversible hydrogen electrode (RHE) scale using the following mathematical relation:

$$E_{RHE} = E_{Ag/Ag2SO4} + 0.059 * pH + E^{0}_{Ag/Ag2SO4} \qquad \text{(S1)}$$

where, E_{RHE} is the RHE potential, $E^{0}_{Ag/Ag2SO4}$= 0.72 V at 25 °C, $E_{Ag/Ag2SO4}$ is the potential measured against the Ag/Ag_2SO_4 reference electrode, and pH is the pH of the used electrolyte.

The turnover frequency (TOF) value was calculated using the following equation,

$$TOF = \frac{J \times A}{2 \times F \times Ns} \qquad (S2)$$

where J and A are the current density of electrocatalyst at a particular overpotential (A/cm^2) and active area of working electrode (cm^2) while F and Ns are the faraday constant (96485 C/mol) and concentration of active sites of electrocatalyst (mol/cm^2) deposited on stainless steel electrode. For HER, N_S was estimated by CV measurements at different scan rates. CV area is plotted against scan rate, and slope exhibits the linear relationship with scan rate. Finally, Ns is calculated by using following mathematical relation,

$$Slope = n^2F^2AN_S/4RT \qquad \text{(S3)}$$

where n, R, and T represent the number of electrons transferred, ideal gas constant and absolute temperature.[S1-S2]

V. SEM analysis of pristine as well as N/S co-doped hierarchical porous carbon

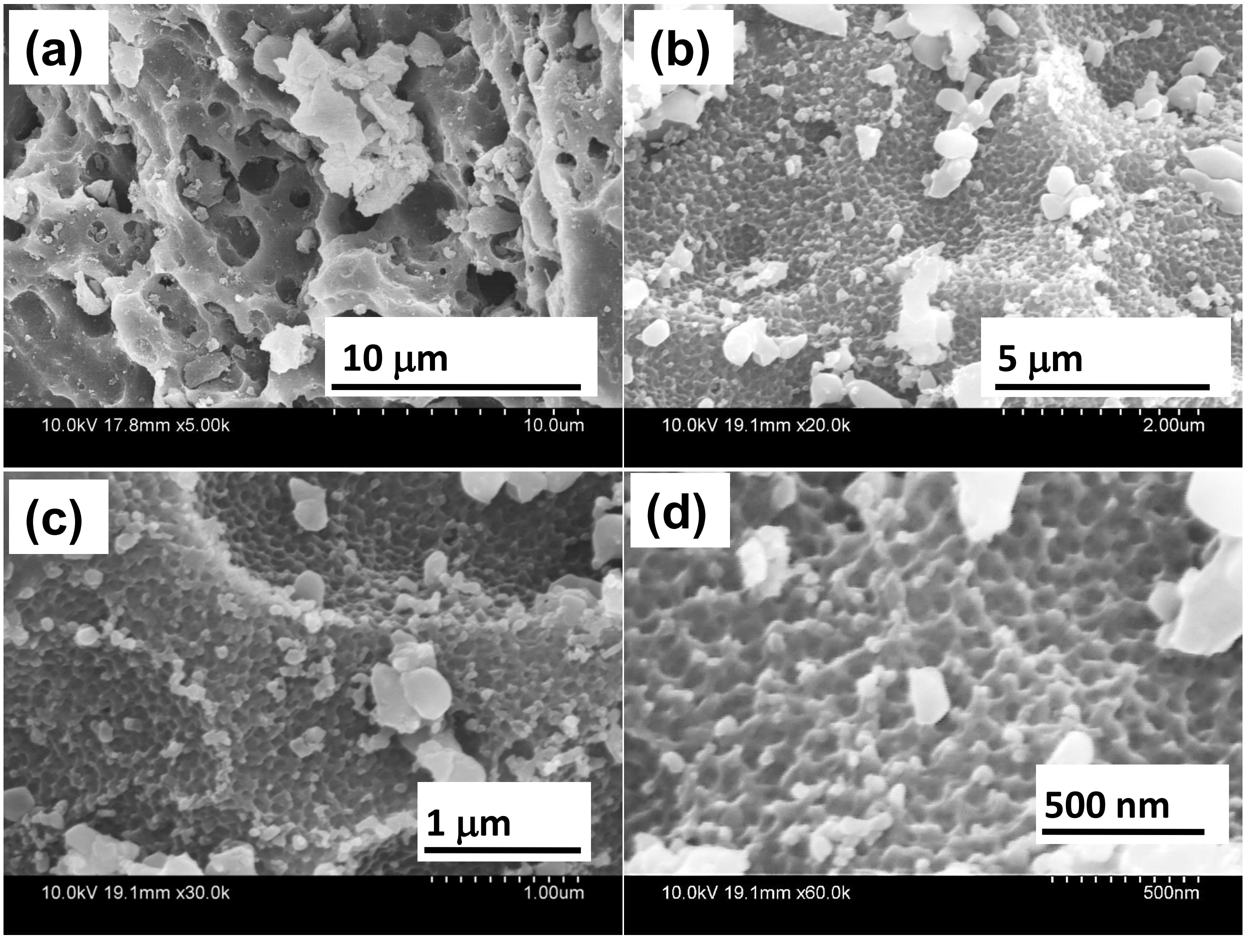

Figure S2. SEM images (a-d) show the morphological features of pristine hierarchical porous carbon at different magnifications.

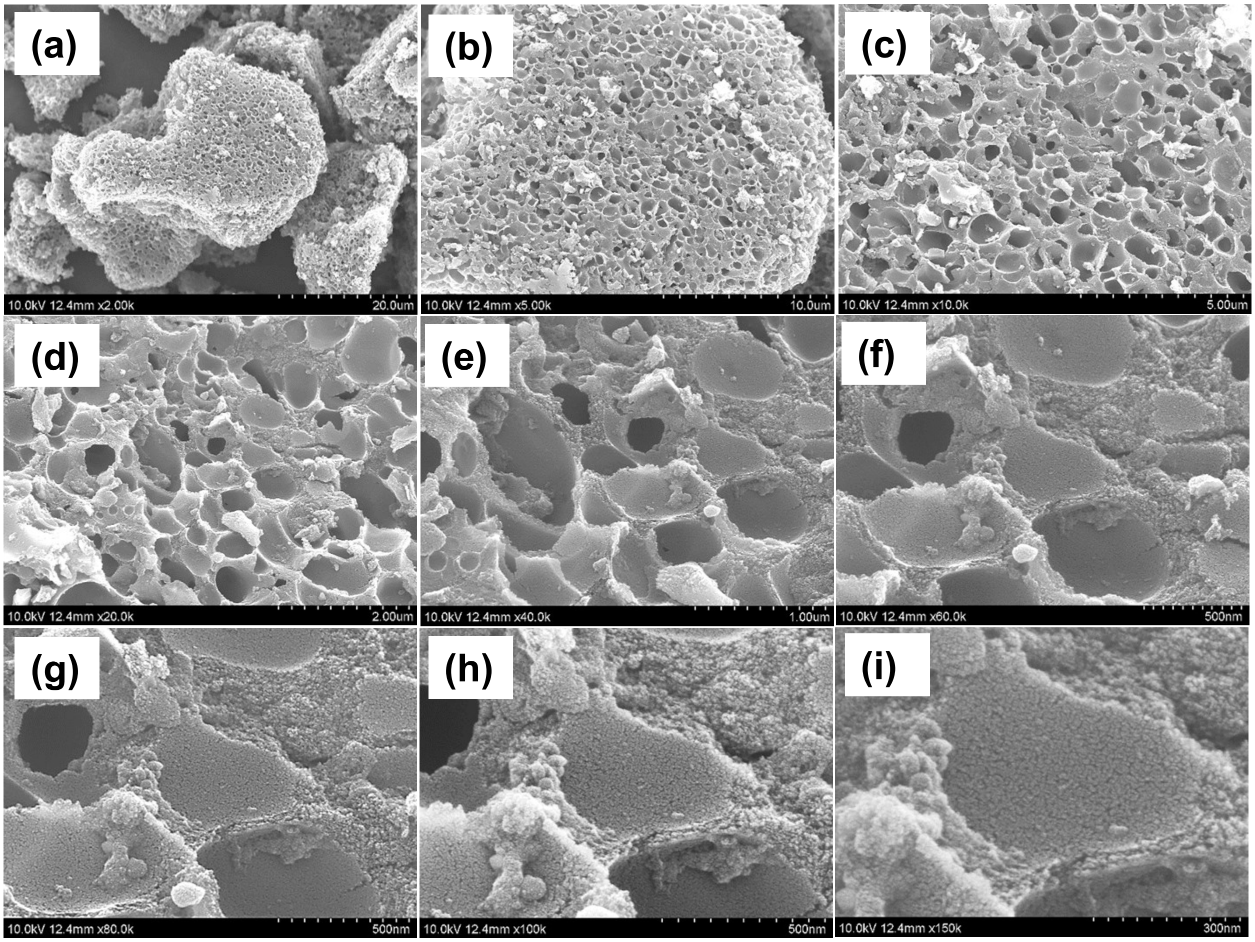

Figure S3. SEM images (a-d) show the morphological features of N/S co-doped hierarchical porous carbon at different magnifications.

VI. TEM-EDX and STEM mapping analysis of N/S co-doped hierarchical porous carbon

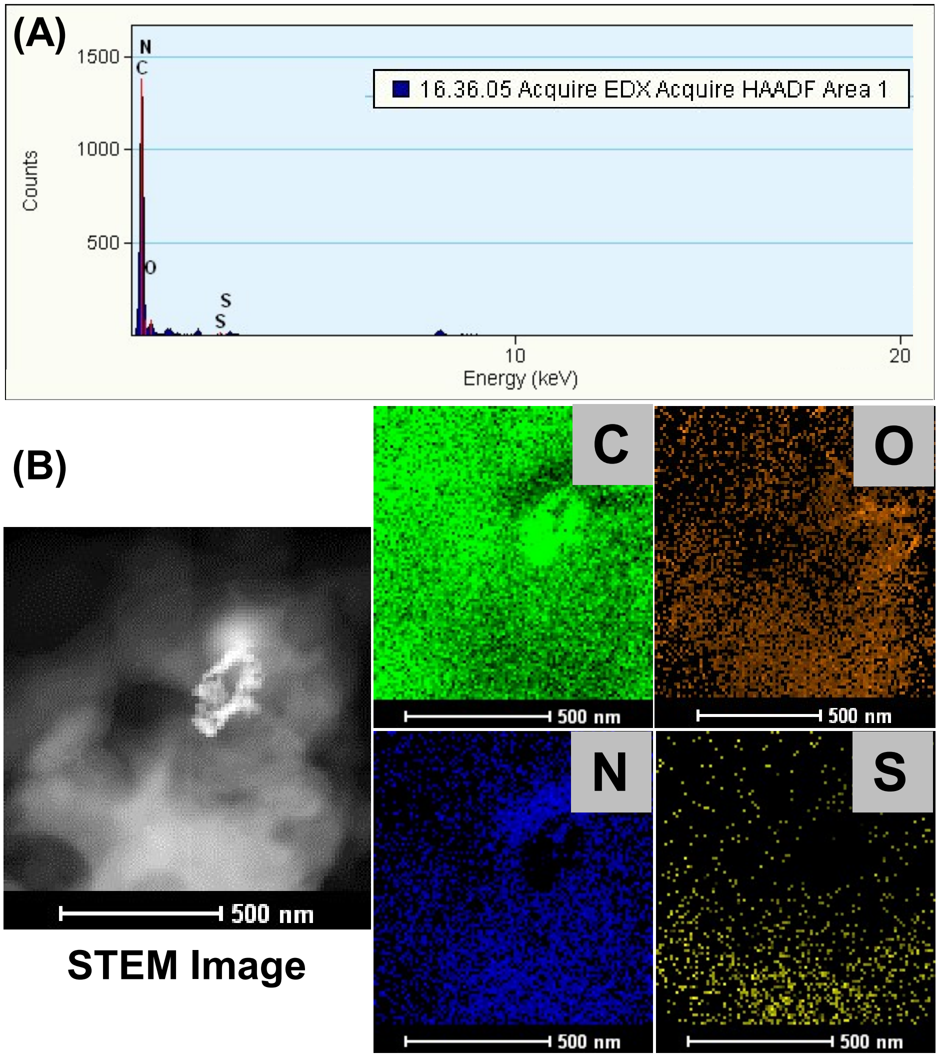

Figure S4. Trace (A) and (B) depict TEM-EDX and STEM analysis of N/S co-doped hierarchical porous carbon.

VII. XPS survey spectra of N/S co-doped hierarchical porous carbon

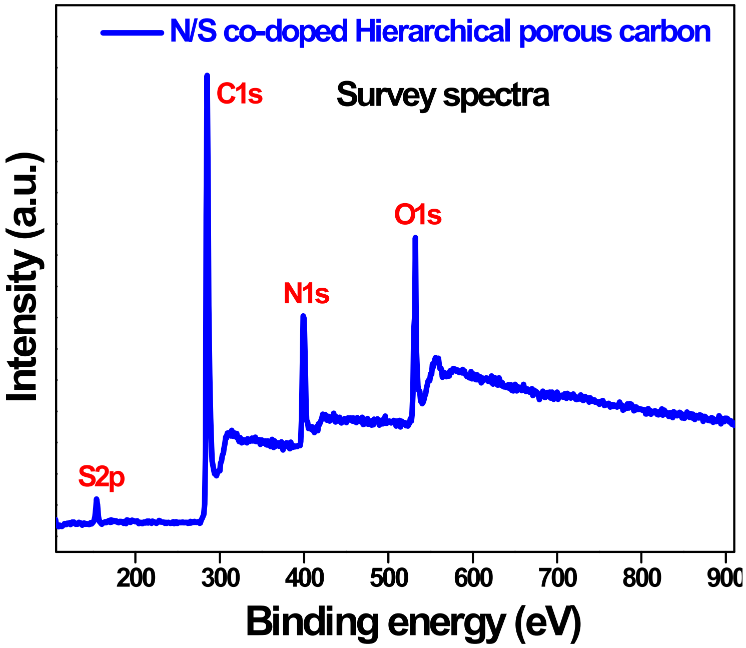

Figure S5. XPS survey spectrum of N/S co-doped hierarchical porous carbon.

VIII. XPS analysis of pristine hierarchical porous carbon

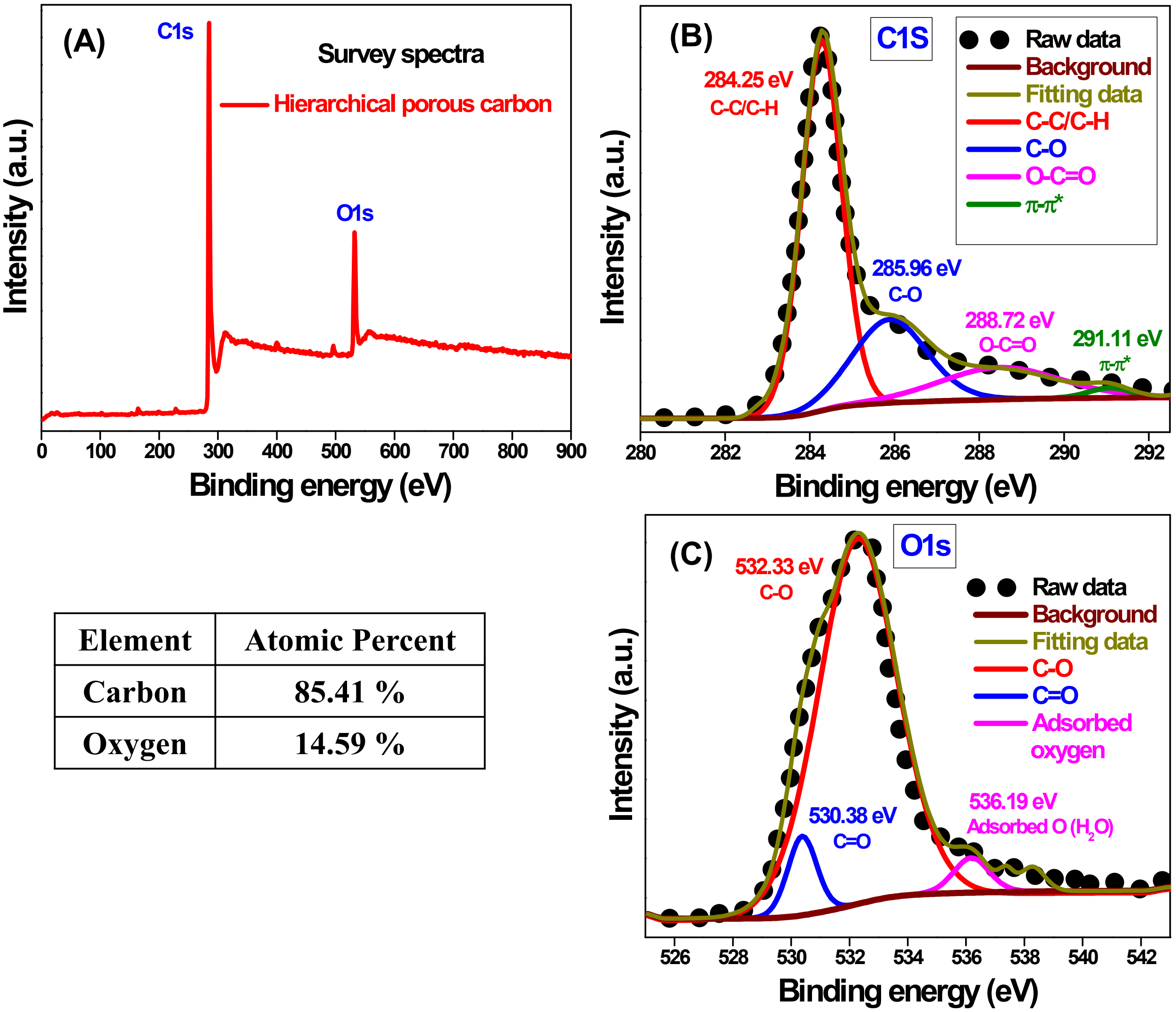

Element	Atomic Percent
Carbon	85.41 %
Oxygen	14.59 %

Figure S6. Trace (A) denotes the XPS survey spectrum of pristine hierarchical porous carbon while traces (B) and (C) show XPS-core spectrum of C1s and O1s respectively.

IX. Fourier Transform Infra-Red (FT-IR) spectroscopic analysis:

Presence of chemical functionalities in both the electrocatalysts is studied by analyzing the FT-IR spectra. Figure S7 shows FT-IR spectra for pristine hierarchical porous carbon (red line) and N/S co-doped hierarchical porous carbon (blue line). In the FT-IR spectrum of pristine material (red line), IR peaks at 2984 cm^{-1} and 2662 cm^{-1} are assigned to the asymmetric and symmetric C-H bond stretching vibrations respectively while peak at 2083 cm^{-1} correspond to C-

H bond of aldehyde group. IR peaks at 1570 cm^{-1} and 971 cm^{-1} are ascribed to C=C stretching and bending vibrations of sp^2 hybridized aromatic carbon. As-mentioned in synthetic protocol, both the samples are activated in presence of air stabilized thermal treatment. So, oxygen functionalities like O-C=O, C=O, C-O (aromatic) and C-O (aliphatic) are appeared at 2317 cm^{-1}, 1715 cm^{-1}, 1298 cm^{-1} and 1187, 1138 cm^{-1} respectively.

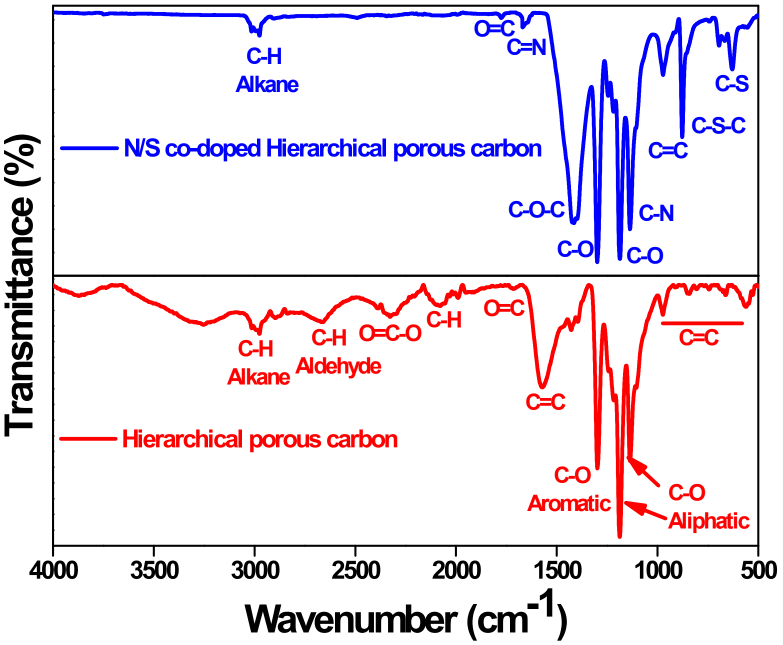

Figure S7. FT-IR spectra of pristine (red line) as well as N/S co-doped hierarchical porous carbon (blue line).

In case of heteroatom-doped sample, we observed similar IR bands related to all functionalities of carbon and oxygen. Nitrogen and sulfur doping in pristine hierarchical porous carbon is confirmed by IR bands centered at 1656 cm^{-1} and 1135 cm^{-1} which are corresponding to C=N and C-N stretching vibration modes, and the IR peaks centered at 876 cm^{-1} and 629 cm^{-1} are assigned to C-S-C and C-S stretching vibrations respectively. All IR peaks related to various functionalities in both the samples are well consistent with XPS analysis.

X. Thermogravimetric analysis (TGA):

Figure S8 demonstrate the thermogravimetric analysis of as-synthesized materials, recorded in the temperature range of 20 to 1000 °C at a heating rate of 10 °C min^{-1} under nitrogen atmosphere.

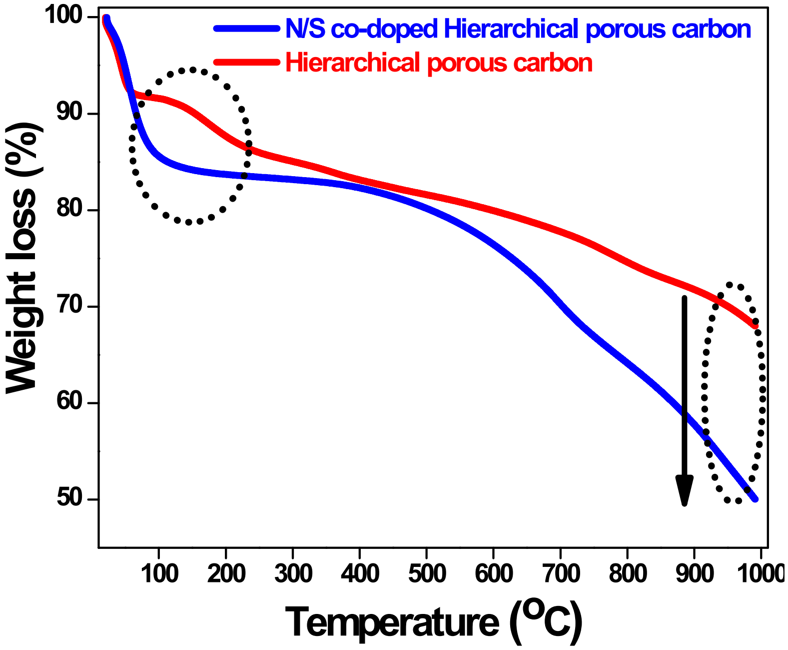

Figure S8. TGA curve of pristine (red line) as well as N/S co-doped hierarchical porous carbon (blue line).

TGA plot of pristine hierarchical porous carbon shows the remarkable thermal stability upto 300 °C, indicating the absence of any organic impurity related to biomass precursor; alginic acid. Moreover, minimal reduction in its actual sample weight is noticed with gradual temperature increment upto 1000 °C. TGA profile of N/S co-doped hierarchical porous carbon reveals the sudden loss of weight in range of 100-200 °C, attributed to the removal of sulfur containing moieties. Furthermore, we notice regular decrement of sample weight with respect to temperature increment due to presence of nitrogen and sulfur containing functionalities in doped sample.

XI. Cyclic Voltammetric analysis of pristine hierarchical porous carbon

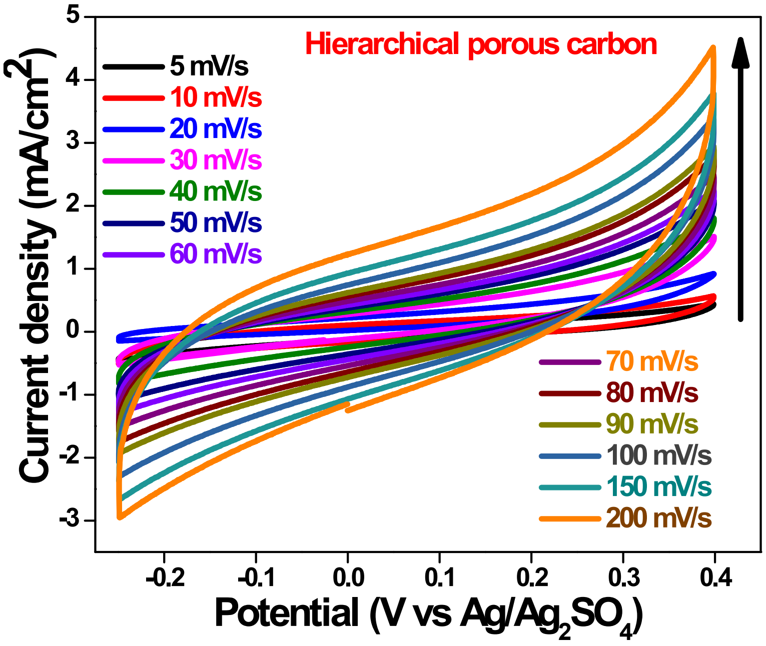

Figure S9. Cyclic voltammogram of pristine hierarchical porous carbon.

XII. Cyclic voltammogram and galvanostatic charging-discharging curve (GCD) of N/S co-doped hierarchical porous carbon in alkaline electrolyte

We have performed the cyclic voltammogram (CV) and galvanostatic charging-discharging curve (GCD) of N/S co-doped hierarchical porous carbon based active electrode material in presence of alkaline (1M KOH) electrolyte at different scan rates and current densities in the potential range of -0.3 to 0.2 V vs. Hg/HgO, which are depicted in the figure S10 (A) and (B). In figure S10 (A), we have noticed the rectangular shape without any proper oxidation and reduction peaks in CV, suggesting the capacitive nature of the synthesized material. Area under CV plot is increased with the scan rate from 5 to 200 mV/s, inferred the faster Faradaic reaction on the surface. More protons approach the electrode surface at a slow scan rate which is responsible for attaining the high capacitance while fewer protons reach at the surface at a high scan rate, resulting in smaller specific capacitance.

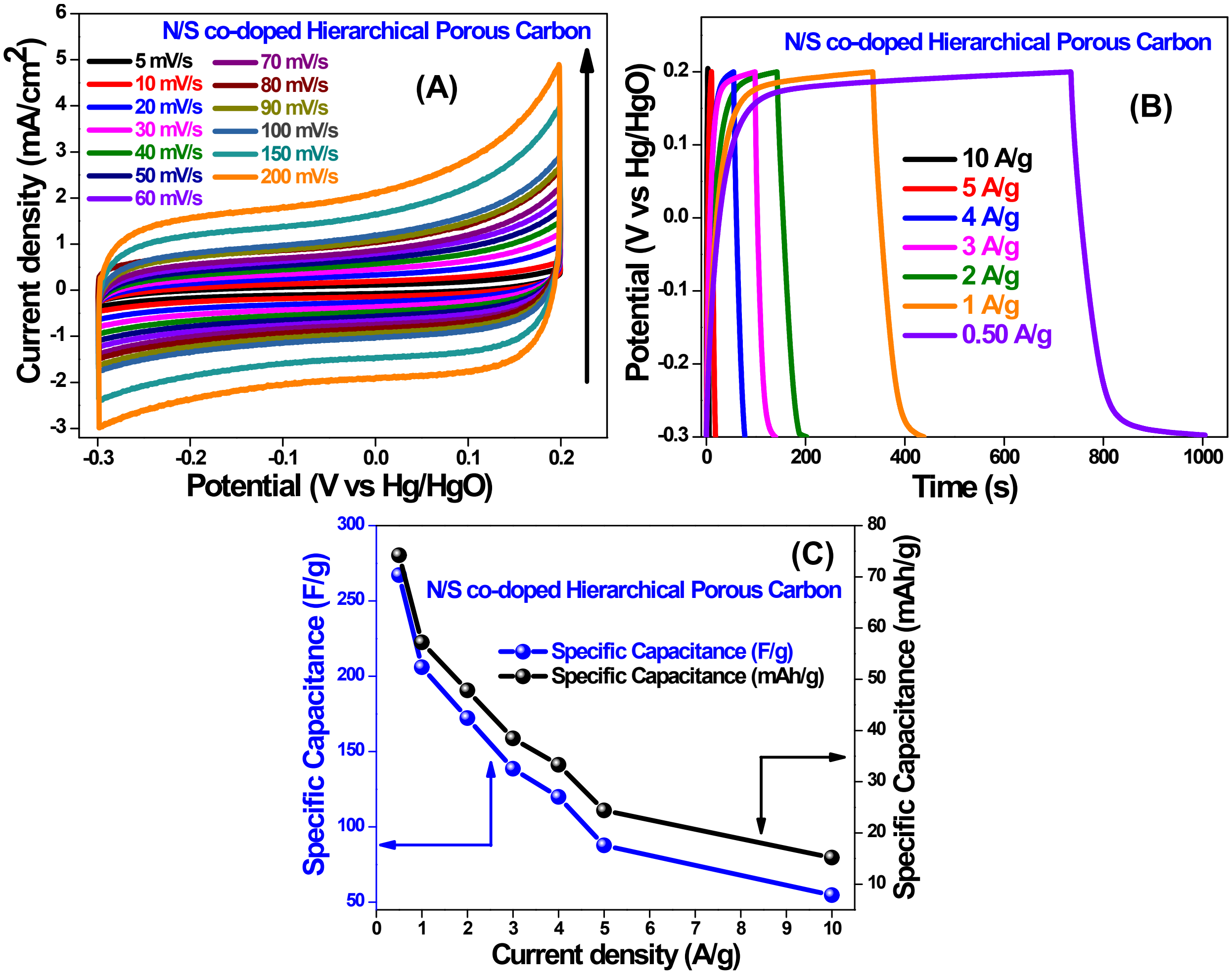

Figure S10. Trace (A) represents the CV curves of N/S co-doped hierarchical porous carbon at the different scan rates using Hg/HgO as reference electrode in an alkaline electrolyte. Traces (B) shows the GCD curves of N/S co-doped hierarchical porous carbon at the different current density values, while traces (C) depicts the variation of calculated specific capacitance with respect to different current density values.

From figure S10 (B), GCD measurements have been carried out at different current densities such as 0.50, 1, 2, 3, 4, 5 and 10 A/g in the potential range of -0.3 to 0.2 V vs. Hg/HgO in an alkaline electrolyte medium. We have noticed the symmetrical triangular shapes of the GCD curves; corroborate the capacitive behavior of the active electrode material. Specific capacitance

(Cs) of the active electrode materials (F/g) are estimated from the discharging curves using the following equation (1).

$$Cs = \frac{I * \Delta t}{m * \Delta V} \qquad (1)$$

where, I is the discharge current (A), Δt is the discharge time interval (s), m is the weight of the active material (g), and ΔV is the applied potential window (V).

Estimated specific capacitance of N/S co-doped hierarchical porous carbon are 267.18 (74.19), 205.98 (57.20), 172.24 (47.83), 138.54 (38.47), 119.92 (33.30), 87.80 (24.38) and 54.64 (15.17) F/g (mAh/g) at current densities of 0.5, 1, 2, 3, 4, 5 and 10 A/g, respectively and the corresponding graphs are shown in figure S10 (C). From the results, specific capacitances of N/S co-doped HPC increase with decrease in current density from 10 to 0.5 A/g, suggesting better redox kinetics at high current density.

XIII. **Table S1:** Summary of supercapacitor performance based on pristine as well as heteroatom (N/S) co-doped hierarchical porous carbon

Sample	**Specific Capacitance (F/g)**	**Electrolyte Medium**	**Reference**
Corncob residue derived porous carbon	120 at 1 A/g	6M KOH	**S3**
Cotton fabric derived hierarchical porous carbons	180 at 0.5 A/g	6M KOH	**S4**
Lignin-based hierarchical porous carbons	224 at 1 A/g	1M H_2SO_4	**S5**
Bamboo derived porous carbon	262 at 0.5 A/g	1M H_2SO_4	**S6**
Walnut Shell-derived hierarchical porous carbon	262 at 0.5 A/g	6M KOH	**S7**
N,S-doped mesoporous carbons	156 at 1 A/g	1M H_2SO_4	**S8**
N/S-doped Porous carbon nanosheets	275 at 0.5 A/g	6M KOH	**S9**

N,S co-doped graphene framework	233 at 1 A/g	0.1M KOH	**S10**
N-S co-doped hierarchical porous carbons	244 at 0.2 A/g	6M KOH	**S11**
N, S-doped activated carbon	264 at 0.25 A/g	6M KOH	**S12**
N/S co-doped hierarchically porous carbon	272 at 1 A/g	6M KOH	**S13**
N, S co-doped hierarchical porous carbon rods	282 at 1 A/g	6M KOH	**S14**
N, S-doped porous nanosheets	298 at 0.5 A/g	6M KOH	**S15**
Pristine hierarchical porous carbon	**231 at 0.5 A/g**	**1M H_2SO_4**	**This Work**
N/S co-doped hierarchical porous carbon	**307 at 0.5 A/g**	**1M H_2SO_4**	**This Work**

XIV. **Table S2.** Comparative analysis of charge-discharge profile of pristine as well as N/S co-doped hierarchical porous carbon with earlier reported **commercial cathodic carbon based materials**.

Commercialized active carbon material	Specific capacitance	References
Norit Super 50	119 F/g at 1A/g	S16
YP-50 (Kuraray)	138 F/g at 1A/g	S17
PX-21	240 F/g at 1A/g	S18
RP-20 (Kuraray)	240 F/g at 1A/g	S19
Maxsorb (Kansai)	321 F/g at 1A/g	S20
Hierarchical porous carbon	231 F/g at 0.5 A/g	Present work
N/S co-doped hierarchical porous carbon	307 F/g at 0.5 A/g	Present work

References:

S1. H. Han, H. Choi, S. Mhin, Y. Hong, K. Kim, J. Kwon, G. Ali, K. Y. Chung, M. Je, H. N. Umh, D.-H. Lim, K. Davey, S.-Z. Qiao, U. Paik and T. Song, *Energy Environ. Sci.*, 2019, **12**, 2443-2454.

S2. Z. Pu, Q. Liu, A. M. Asiri, A. Y. Obaid and X. Sun, *J. Power Sources*, 2014, **263**, 181-185.

S3. Q. Wen-Hui, X. Yuan-Yuan, L. An-Hui, Z. Xiang-Qian and L. Wen-Cui, *Bioresour. Technol.*, 2015, **189**, 285-291.

S4. L. Chen, T. Ji, L. Mu and J. Zhu, *Carbon*, 2017, **111**, 839-848.

S5. D. Salinas-Torres, R. Ruiz-Rosas, M. J. Valero-Romero, J. Rodríguez-Mirasol, T. Cordero, E. Morallón and D. Cazorla-Amorós, *J. Power Sources*, 2016, **326**, 641-651.

S6. H. Chen, D. Liu, Z. Shen, B. Bao, S. Zhao and L. Wu, *Electrochim. Acta*, 2015, **180**, 241-251.

S7. H. Fu, L. Chen, H. Gao, X. Yu, J. Hou, G. Wang, F. Yu, H. Li, C. Fan, Y.-l. Shi and X. Guo, *Int. J. Hydrog. Energy*, 2020, **45**, 443-451.

S8. S. Zhang, A. Ikoma, K. Ueno, Z. Chen, K. Dokko and M. Watanabe, *ChemSusChem*, 2018, **8**, 1608-1617.

S9. T. Wei, X. Wei, L. Yang, H. Xiao, Y. Gao and H. Li, *J. Power Sources*, 2016, **331**, 373-381.

S10. L. Chen, M. Shi, B. He, M. Zhou, C. Xu, Z. Chen, Y. Kuang, *J. Mater. Res.*, 2019, **34**, 1993-2002.

S11. F. Liu, Z. Wang, H. Zhang, L. Jin, X. Chu, B. Gu, H. Huang, W. Yang, *Carbon*, 2019, **149**, 105-116.

S12. W. Si, J. Zhou, S. Zhang, S. Li, W. Xing and S. Zhuo, *Electrochim. Acta*, 2013, **107**, 397-405.

S13. S. Huo, M. Liu, L. Wu, M. Liu, M. Xu, W. Ni and Y.-M. J. Yan, *J. Power Sources*, 2018, **387**, 81-90.

S14. L. Miao, D. Zhu, M. Liu, H. Duan, Z. Wang, Y. Lv, W. Xiong, Q. Zhu, L. Li, X. Chai and L. Gan, *Electrochim. Acta*, 2018, **274**, 378-388.

S15. Y. Li, G. Wang, T. Wei, Z. Fan and P. Yan, *Nano Energy*, 2016, **19**, 165-175.

S16. E. Raymundo-Pinero, M. Cadek, and F. Beguin, *Adv. Funct. Mater.*, 2009, **19**, 1032-103.

S17. Y. Qing, Y. Jiang, H. Lin, L. Wang, A. Liu, Y. Cao, R. Sheng, Y. Guo, C. Fan, S. Zhang, D. Jia and Z. Fan, *J. Mater. Chem. A*, 2019, **7**, 6021-6027.

S18. K. Kierzek, E. Frackowiak, G. Lota, G. Gryglewicz and J. Machnikowski, *Electrochim. Acta*, 2004, **49**, 515-523.

S19. A. Janes, H. Kurig and E. Lust, *Carbon*, 2007, **45**, 1226-1233.

S20. B. Xing, G. Huang, L. Chen, H. Guo, C. Zhang, W. Xie and Z. Chen, *J. Porous Mater.*, 2016, **23**, 67-73.